

THE WEAKLY NONLINEAR MAGNETOROTATIONAL INSTABILITY

CLARK, S.E.¹ AND OISHI, J.S.^{2,3}

Draft version August 5, 2016

ABSTRACT

We conduct a formal weakly nonlinear analysis of the magnetorotational instability (MRI) in a Taylor Couette flow. This is a multiscale perturbative treatment of the nonideal, axisymmetric MRI near threshold, subject to realistic radial boundary conditions. We analyze both the standard MRI, initialized by a constant vertical background magnetic field, and the helical MRI, in which the base magnetic field contains an azimuthal component. We find that the evolution of the weakly nonlinear perturbation amplitude of the standard MRI is described by a real Ginzburg-Landau equation (GLE), while the amplitude of the helical MRI takes the form of a complex GLE.

1. INTRODUCTION

The magnetorotational instability (MRI) drives angular momentum transport and turbulence in astrophysical disks. Its discovery by [Balbus & Hawley \(1991\)](#); actually a rediscovery of [Chandrasekhar 1960](#)) was a breakthrough in the longstanding question of how efficient accretion can exist in the universe: that is, how matter collapsing onto a central body is able to coalesce despite the conservation of specific angular momentum. The ubiquity of astrophysical disks suggests that systems both experience and overcome this centrifugal barrier, and accretion proceeds even in hydrodynamically stable disks. The MRI is excited by weak magnetic fields in differentially rotating fluids, and since its discovery it has been widely invoked to explain accretion in protoplanetary disks (see [Armitage 2010](#) and references therein), binary systems (), and disks around black holes (), as well as jet and wind launching ([Lesur et al. 2013](#)), dynamos, etc (cite these)

Although the MRI is broadly important to many astrophysical systems, its general properties, and in particular its nonlinear saturation mechanism, remain poorly understood. The diversity of astrophysical systems which may permit the MRI admits an enormous parameter space to be explored. In protoplanetary disks, for example, the behavior and evolution of the MRI may change drastically depending on the properties of the magnetic field, the disk composition, disk geometry, etc. Numerical simulation of realistic disk physics is currently an area of intense focus, and is enabling the study of nonideal MHD effects, disk stratification, nonequilibrium chemistry, and other complex physics that does not lend itself easily to analytic study. Still, computational costs inevitably constrain numerical approaches. MRI saturation is a complicated nonlinear problem which may depend on the assumptions and approximations adopted by simulations in nonobvious ways. Analytic methods can play a powerful role

Because of the MRI’s complexity, analytical treatments of the MRI use some combination of convenient

approximations, such as ideal MHD, linearized equations, expedient boundary conditions, and simplified geometries. In particular, much of the analytical work on MRI saturation has focused on local approximations, often representing a section of a disk by solving the MHD equations in an isolated region subject to shear periodic boundary conditions (the “shearing box”). The shearing box is an inexpensive computational framework, so is used by many numerical MRI studies as well. However, while the MRI is a local instability, certain properties of the local problem are not generic to the global problem. In the shearing box, linear evolution is dominated by a class of MRI mode known as channel modes. These are linear modes which also happen to be exact solutions to the *nonlinear* local MRI equations. Runaway growth is avoided in this paradigm by the instability of the channel modes themselves, which are destroyed by parasitic (secondary) instabilities ([Goodman & Xu 1994](#), [Pessah 2010](#)). The growth of parasitic modes provides a saturation avenue for channel mode-dominated flows, yet this is unlikely to be the dominant saturation mechanism in laboratory experiments or astrophysical disks, as channel modes are artificially over-prominent in the shearing box (e.g. [Latter et al. 2015](#)).

The theory we develop here employs realistic radial boundary conditions, and so MRI modes are global and channel modes are not present. A number of saturation mechanisms have been proposed for the MRI which do not rely on channel modes dominating the flow. The MRI feeds off of the free energy from differential rotation, and so a modification of the background shear may cause saturation (e.g. [Knobloch & Julien 2005](#), [Umurhan et al. 2007b](#)). The MRI may transfer its free energy into the magnetic field, and saturate when the field is too strong to be susceptible to the MRI (e.g. [Ebrahimi et al. 2009](#)). The MRI may saturate differently depending on the particular parameter regime under investigation, and so our challenge is not only in identifying possible saturation mechanisms, but in understanding how and when each applies in different astrophysical environments.

Our investigation is astrophysically motivated, but we also intend our theory to be relevant to laboratory experiments. Several experimental efforts are attempting to observe the MRI in the laboratory, which would allow the study of a crucial astrophysical phenomenon in a controlled setting. Unfortunately, detection of the MRI

¹ Department of Astronomy, Columbia University, New York, NY

² Department of Astrophysics, American Museum of Natural History, New York, NY

³ Department of Physics, SUNY Farmingdale

has so far proven elusive. [Sisan et al. 2004](#) claimed to detect the MRI in a spherical Couette flow, but most likely detected unrelated MHD instabilities instead ([Hollerbach 2009](#), [Gissinger et al. 2011](#)). Most relevant to our work is the Princeton Plasma Physics Laboratory (PPPL) MRI Experiment, a liquid gallium Taylor-Couette flow exposed to an axial magnetic field ([Ji et al. 2001](#)). Some theoretical work designed to complement the Princeton MRI experiment involves direct simulation of the experimental conditions, much of it focused on the specific challenges in identifying MRI signatures despite apparatus-driven spurious flows (e.g. [Gissinger et al. 2012](#)). In particular, the vertical endcaps on a laboratory MRI apparatus drives meridional flows which both inhibit the excitement of MRI and obscure its detection. The Princeton MRI experiment employs split, independently rotating endcaps to mitigate these flows ([Schartman et al. 2009](#)). Our work here assumes an infinite vertical domain, an idealization that is theoretically expedient but experimentally impractical. However, our setup is designed to be an accurate treatment of the radial dimension of the flow in a Taylor Couette apparatus like the one used in the Princeton MRI experiment.

Many investigations of the MRI use the “narrow gap” approximation, in which the radial extent of the fluid channel is taken to be much smaller than the radius of curvature. That is, for a channel center r_0 bounded by inner and outer radii r_1 and r_2 , respectively, the narrow gap approximation applies when $r_0 \gg (r_2 - r_1)$. The narrow gap approximation simplifies the MRI equations by excluding curvature terms, because the flow through a narrow gap can be taken to be approximately linear in ϕ , i.e. Cartesian. Previous investigations into the weakly nonlinear MRI have used this narrow gap approximation ([Umurhan et al. 2007a](#), [Umurhan et al. 2007b](#), [Clark & Oishi 2016a](#)). In this work we undertake the first (to our knowledge) weakly nonlinear analysis of the MRI in the wide gap regime, where the channel width may be comparable to or larger than its distance from the center of rotation.

Because we include curvature terms, our theory is also relevant to the helical magnetorotational instability (HMRI). Discovered by [Hollerbach & Rüdiger \(2005\)](#), the HMRI is an overstability in which the background magnetic field is helical. The HMRI currently occupies a special place in the MRI puzzle. The HMRI has been proposed as a method of awakening angular momentum transport in the “dead zones” of protoplanetary disks where the magnetic Prandtl number ($Pm = \nu/\eta$) becomes very small. However the rotation profiles needed to excite HMRI may be prohibitively steeper than Keplerian depending on the boundary conditions, and so its role in astrophysical disks is currently debated ([Liu et al. 2006](#), [Rüdiger & Hollerbach 2007](#), [Kirillov & Stefani 2013](#)). The HMRI is significantly easier to excite in a laboratory setting than the standard MRI, and has already been detected in the laboratory by the Potsdam Rossendorf Magnetic Instability Experiment (PROMISE; [Stefani et al. 2006](#), [Stefani et al. 2009](#)).

We explore the weakly nonlinear HMRI

2. WIDE GAP EQUATIONS

The basic equations solved are the momentum and induction equations,

$$\partial_t \mathbf{u} + \mathbf{u} \cdot \nabla \mathbf{u} = -\frac{1}{\rho} \nabla P - \nabla \Phi + \frac{1}{\rho} (\mathbf{J} \times \mathbf{B}) + \nu \nabla^2 \mathbf{u} \quad (1)$$

and

$$\partial_t \mathbf{B} = \nabla \times (\mathbf{u} \times \mathbf{B}) + \eta \nabla^2 \mathbf{B}, \quad (2)$$

where P is the gas pressure, ν is the kinematic viscosity, η is the microscopic diffusivity, $\nabla \Phi$ is the gravitational force per unit mass, and the current density is $\mathbf{J} = \nabla \times \mathbf{B}$. We solve these equations subject to the incompressible fluid and solenoidal magnetic field constraints,

$$\nabla \cdot \mathbf{u} = 0 \quad (3)$$

and

$$\nabla \cdot \mathbf{B} = 0. \quad (4)$$

We perturb these equations axisymmetrically in a cylindrical (r, ϕ, z) geometry, i.e. $\mathbf{u} = \mathbf{u}_0 + \mathbf{u}_1$ and $\mathbf{B} = \mathbf{B}_0 + \mathbf{B}_1$, where \mathbf{u}_0 and \mathbf{B}_0 are defined below. We define a Stokes stream function Ψ such that

$$\mathbf{u}_1 = \begin{bmatrix} \frac{1}{r} \partial_z \Psi \hat{\mathbf{r}} \\ u_\phi \hat{\phi} \\ -\frac{1}{r} \partial_r \Psi \hat{\mathbf{z}} \end{bmatrix}, \quad (5)$$

and define the magnetic vector potential A analogously. These definitions automatically satisfy Equations 3 and 4 for axisymmetric disturbances. We note that in the linearized equations, streamfunctions of the form $u_x = \partial_z \Psi$, $u_z = -(\partial_r + \frac{1}{r})\Psi$, and the corresponding definitions of the magnetic vector potential, are convenient choices, but this does not hold true for the nonlinear terms because of the incommutability of ∂_r and $\partial_r + \frac{1}{r}$.

The astrophysical magnetorotational instability operates in accretion disks and in stellar interiors, environments where fluid rotation is strongly regulated by gravity. In accretion disks, differential rotation is imposed gravitationally by a central body, so the rotation profile is forced to be Keplerian. Clearly a gravitationally enforced Keplerian flow is inaccessible to laboratory study, so differential rotation is created by rotating an inner cylinder faster than an outer cylinder (a Taylor-Couette setup). For a nonideal fluid subject to no-slip boundary conditions, the base flow is

$$\Omega(r) = a + \frac{b}{r^2}, \quad (6)$$

where $a = (\Omega_2 r_2^2 - \Omega_1 r_1^2)/(r_2^2 - r_1^2)$, $b = r_1^2 r_2^2 (\Omega_1 - \Omega_2)/(r_2^2 - r_1^2)$, and Ω_1 and Ω_2 are the rotation rates at the inner and outer cylinder radii, respectively. In the laboratory, r_1 and r_2 are typically fixed by experimental design. However Ω_1 and Ω_2 may be chosen such that the flow in the center of the channel is approximately Keplerian. Defining a shear parameter q , we see that for Couette flow,

$$q(r) \equiv -\frac{d \ln \Omega}{d \ln r} = \frac{2b}{ar^2 + b}. \quad (7)$$

TABLE 1
FIDUCIAL PARAMETERS FOR MRI RUNS

	ξ	Pm	β	Ω_2/Ω_1	R_1/R_2	radial magnetic b.c.
Standard MRI	0	1E-3	25	0.18	0.33	conducting
Helical MRI	4	1E-6	1.7E-2	0.27	0.5	insulating

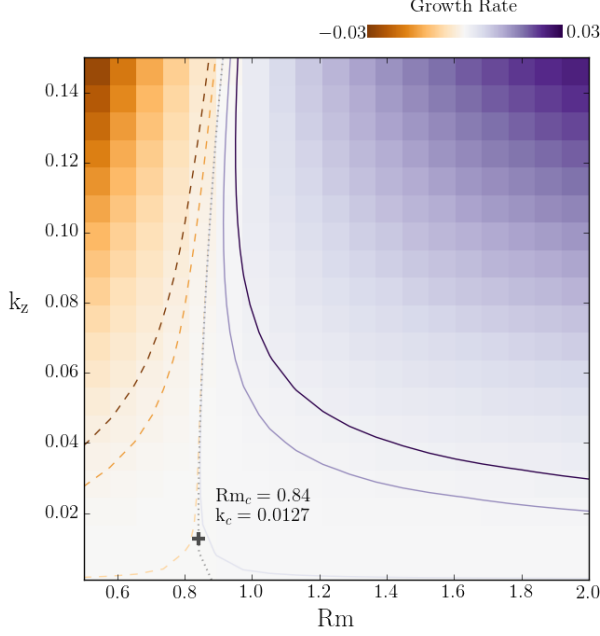


FIG. 1.— Growth rates in the (Rm, k_z) plane. Color map shows growth rate found by solving the linear eigenvalue problem for each (Rm, k_z) in the grid. The eigenvalue problem was solved for the widegap parameters listed in Table 1. Overlaid contours show growth rates at $[-2E-3, -1E-3, -1E-5, 1E-5, 1E-3, 2E-3]$, where dashed contours represent negative values. The gray dotted line shows the interpolated marginal stability curve. The critical parameters $Rm_c = 0.84$ and $k_c = 0.0127$ correspond to the smallest parameter values that yield a zero growth rate.

Thus through judicious choice of cylinder rotation rates, we can set $q(r_0) = 3/2$, for quasi-Keplerian flow. Note that the narrow gap approximation imposes a linear shear (constant q). Our base velocity is $\mathbf{u}_0 = r\Omega(r)\hat{\phi}$. We initialize a magnetic field $\mathbf{B}_0 = B_0\hat{\mathbf{z}} + B_0\xi\frac{r_0}{r}\hat{\phi}$, so that the base magnetic field is axial when $\xi = 0$ and otherwise helical.

In this work we will focus our findings on two fiducial parameter sets, one for the standard MRI (hereafter SMRI) where $\xi = 0$ and one for the helical MRI (hereafter HMRI). We choose the SMRI parameters to be comparable to the case explored in [Umurhan et al. 2007b](#), with the geometric parameters of [Goodman & Ji 2002](#). The HMRI parameters were chosen to be comparable to [Hollerbach & Rüdiger 2005](#). Our fiducial parameters are described in Table 1.

Our perturbed system is

$$\frac{1}{r}\partial_t(\nabla^2\Psi - \frac{2}{r}\partial_r\Psi) - \frac{2}{\beta}\frac{1}{r}B_0\partial_z(\nabla^2A - \frac{2}{r}\partial_rA) - \frac{2}{r}u_0\partial_zu_\phi + \frac{2}{\beta}\frac{2}{r^2}B_0\xi\partial_zB_\phi - \frac{1}{\text{Re}}\left[\nabla^2(\frac{1}{r}\nabla^2\Psi) - \frac{1}{r^3}\partial_r^2\Psi - \frac{1}{r^4}\partial_r\Psi\right] = N^{(\Psi)} \quad (8)$$

$$\partial_tu_\phi + \frac{1}{r^2}u_0\partial_z\Psi + \frac{1}{r}\partial_ru_0\partial_z\Psi - \frac{2}{\beta}B_0\partial_zB_\phi - \frac{1}{\text{Re}}(\nabla^2u_\phi - \frac{1}{r^2}u_\phi) = N^{(u)} \quad (9)$$

$$\partial_tA - B_0\partial_z\Psi - \frac{1}{\text{Rm}}(\nabla^2A - \frac{2}{r}\partial_rA) = N^{(A)} \quad (10)$$

$$\partial_tB_\phi + \frac{1}{r^2}u_0\partial_zA - B_0\partial_zu_\phi - \frac{1}{r}\partial_ru_0\partial_zA - \frac{2}{r^3}B_0\xi\partial_z\Psi - \frac{1}{\text{Rm}}(\nabla^2B_\phi - \frac{1}{r^2}B_\phi) = N^{(B)} \quad (11)$$

The righthand side of the equations contain the nonlinear terms

$$N^{(\Psi)} = -J(\Psi, \frac{1}{r^2}(\nabla^2\Psi - \frac{2}{r}\partial_r\Psi)) + \frac{2}{\beta}J(A, \frac{1}{r^2}(\nabla^2A - \frac{2}{r}\partial_rA)) - \frac{2}{\beta}\frac{2}{r}B_\phi\partial_zB_\phi + \frac{2}{r}u_\phi\partial_zu_\phi \quad (12)$$

$$N^{(u)} = \frac{2}{\beta}\frac{1}{r}J(A, B_\phi) - \frac{1}{r}J(\Psi, u_\phi) + \frac{2}{\beta}\frac{1}{r^2}B_\phi\partial_zA - \frac{1}{r^2}u_\phi\partial_z\Psi \quad (13)$$

$$N^{(A)} = \frac{1}{r}J(A, \psi) \quad (14)$$

$$N^{(B)} = \frac{1}{r}J(A, u_\phi) + \frac{1}{r}J(B_\phi, \psi) + \frac{1}{r^2}B_\phi\partial_z\psi - \frac{1}{r^2}u_\phi\partial_zA \quad (15)$$

where J is the Jacobian $J(f, g) \equiv \partial_z f \partial_r g - \partial_r f \partial_z g$. Note that in the above, $\nabla^2 f \equiv \partial_r^2 f + \partial_z^2 f + \frac{1}{r} \partial_r f$. Equations 8 - 15 are nondimensionalized, where lengths have been scaled by r_0 , velocities by $r_0 \Omega_0$, densities by ρ_0 , and magnetic fields by B_0 ; where B_0 appears in the above it is formally unity. $\Omega_0 = \Omega(r_0)$ is the rotation rate at the center of the channel. We introduce the Reynolds number $\text{Re} = \Omega_0 r_0^2 / \nu$, the magnetic Reynolds number $\text{Rm} = \Omega_0 r_0^2 / \eta$, and a plasma beta parameter $\beta = \Omega_0^2 r_0^2 \rho_0 / B_0^2$. If we define the dimensional cylindrical coordinate $r = r_0(1 + \delta x)$, the narrow gap equations are recovered in the limit $\delta \rightarrow 0$.

We solve the system subject to periodic vertical boundary conditions and no-slip, perfectly conducting radial boundary conditions, namely

$$\Psi = \partial_r \Psi = u = A = \partial_r(rB) = 0 \quad (16)$$

at $r = r_1, r_2$.

We note that Equations 8 - 11 are written in a non-standard form, with the nonlinear terms on the righthand side. This choice has a practical motivation. As detailed in §3, we expand these equations in a perturbation series and solve them order by order using a pseudospectral code. The code solves partial differential equations of the form $M \partial_t \mathbf{V} + \mathbf{L} \mathbf{V} = \mathbf{F}$, where M and L are matrices and \mathbf{F} is a vector containing any inhomogeneous terms. The nonlinear terms in our perturbation analysis become inhomogeneous term inputs to the solver.

3. WEAKLY NONLINEAR PERTURBATION ANALYSIS

Just as in the weakly nonlinear analyses of [Umurhan et al. 2007b](#) and [Clark & Oishi 2016a](#), we tune the system away from marginality by taking $B_0 \rightarrow B_0(1 - \epsilon^2)$, where $\epsilon \ll 1$. We parameterize scale separation as $Z = \epsilon z$ and $T = \epsilon^2 t$, where Z and T are slowly varying spatial and temporal scales, respectively. We group the fluid variables into a state vector $\mathbf{V} = [\Psi, u, A, B]^T$, such that the full nonlinear system can be expressed as

$$\mathcal{D} \partial_t \mathbf{V} + \mathcal{L} \mathbf{V} + \epsilon^2 \tilde{\mathcal{G}} \mathbf{V} + \xi \tilde{\mathcal{H}} \mathbf{V} + \mathbf{N} = 0, \quad (17)$$

where \mathcal{D} , \mathcal{L} , and $\tilde{\mathcal{G}}$ are matrices defined in Appendix A, and \mathbf{N} is a vector containing all nonlinear terms defined in Appendix B. We then expand the variables in a perturbation series $\mathbf{V} = \epsilon \mathbf{V}_1 + \epsilon^2 \mathbf{V}_2 + \epsilon^3 \mathbf{V}_3 + h.o.t.$. The perturbed system can then be expressed at each order by the equations

$$\mathcal{O}(\epsilon) : \mathcal{L} \mathbf{V}_1 + \xi \tilde{\mathcal{H}} \mathbf{V}_1 + \mathcal{D} \partial_t \mathbf{V}_1 = 0 \quad (18)$$

$$\mathcal{O}(\epsilon^2) : \mathcal{L} \mathbf{V}_2 + \xi \tilde{\mathcal{H}} \mathbf{V}_2 + \tilde{\mathcal{L}}_1 \partial_Z \mathbf{V}_1 + \xi \mathcal{H} \partial_Z \mathbf{V}_1 + \mathbf{N}_2 = 0 \quad (19)$$

$$\begin{aligned} \mathcal{O}(\epsilon^3) : \mathcal{L} \mathbf{V}_3 + \xi \tilde{\mathcal{H}} \mathbf{V}_3 + \mathcal{D} \partial_T \mathbf{V}_1 + \tilde{\mathcal{L}}_1 \partial_Z \mathbf{V}_2 \\ + \xi \mathcal{H} \partial_Z \mathbf{V}_2 + \tilde{\mathcal{L}}_2 \partial_Z^2 \mathbf{V}_1 - \xi \tilde{\mathcal{H}} \mathbf{V}_1 + \tilde{\mathcal{G}} \mathbf{V}_1 + \mathbf{N}_3 = 0. \end{aligned} \quad (20)$$

$$(21)$$

See Appendix A for the definition of matrices and nonlinear vectors, and a thorough derivation. We emphasize that Equations 18 - 21 have the same form as these equations in the narrow gap case, although the matrices (which contain all radial derivatives) are significantly

different in this wide gap formulation. This is because we do not have slow variation in the radial dimension. The slow variation in Z and T are parameterized as an amplitude function $\alpha(Z, T)$ which modulates the flow in these dimensions. This parameterization coupled with the boundary conditions lead us to an ansatz linear solution $\mathbf{V}_1 = \alpha(Z, T) \mathbb{V}_{11}(r) e^{ik_z z} + c.c.$, where the radial variation is contained in \mathbb{V}_{11} .

We solve the equations at each order using Dedalus, an open source pseudospectral code ([Burns et al. in prep.](#)). Because our domain is bounded only radially and not vertically, we solve the radial dimension on a basis of Chebyshev polynomials, and the vertical dimension on a Fourier series basis. We solve Equation 18 as a linear eigenvalue problem, and Equations 20 and 21 as linear boundary value problems. To analyze the MRI system at marginality, we fix the parameters listed in Table 1 and determine the critical Rm and k_z by repeatedly solving Equation 18 to determine the smallest parameter values for which the fastest growing mode is zero. That is, we solve the linear eigenvalue problem for eigenvalues $\sigma = \gamma + i\omega$. Figure 1 shows linear MRI growth rates γ in the (Rm, k_z) plane. For the fiducial standard MRI parameters in Table 1 we find critical parameters $\text{Rm}_c = 0.84$, $k_c = 0.0127$.

The result of the weakly nonlinear analysis is a single amplitude equation for α . This amplitude equation is found by enforcing a solvability criterion on Equation 21. We find

$$\partial_T \alpha = b\alpha + d\partial_Z^2 \alpha - c\alpha |\alpha^2|, \quad (22)$$

a Ginzburg-Landau equation (GLE). The GLE governs the weakly nonlinear amplitude behavior in a wide range of physical systems, including the narrow gap MRI ([Umurhan et al. 2007b](#)), Rayleigh-Bénard convection, and hydrodynamic Taylor Couette flow. We emphasize that this is a model equation, valid only near marginality (e.g. [Cross & Hohenberg 1993](#)). The dynamics of the GLE are determined by its coefficients, which are in turn determined by the linear eigenfunctions and nonlinear vectors plotted in Figures 2 and 3. Equation 22 contains three coefficients: b , which determines the linear growth rate of the system, d , a diffusion coefficient, and c , the coefficient of the nonlinear term. When all of the coefficients of Equation 22 are real, this is known as the real GLE, although the amplitude α remains complex. The real GLE is subject to several well-studied instabilities, including the Ekhaus and Zig-Zag instabilities. When the coefficients are complex, we have the complex GLE, a source of even richer phase dynamics than its real counterpart (e.g. [Aranson & Kramer 2002](#)).

For the standard MRI we derive a real GLE. Here we note a departure from the behavior of the narrow gap system. The purely conducting boundary condition states that the axial component of the current ($\mathbf{J}_z = [\nabla \times \mathbf{B}]_z$) must be zero at the walls. In the thin gap geometry, the purely conducting boundary condition on the azimuthal magnetic field is $\partial_x(B_y) = 0$ for axisymmetric perturbations. A spatially constant azimuthal field satisfies both the thin-gap MRI equations and this boundary condition. This neutral mode is formally included in the analysis of [Umurhan et al. 2007b](#) and yields a second amplitude equation in the form of a simple diffusion

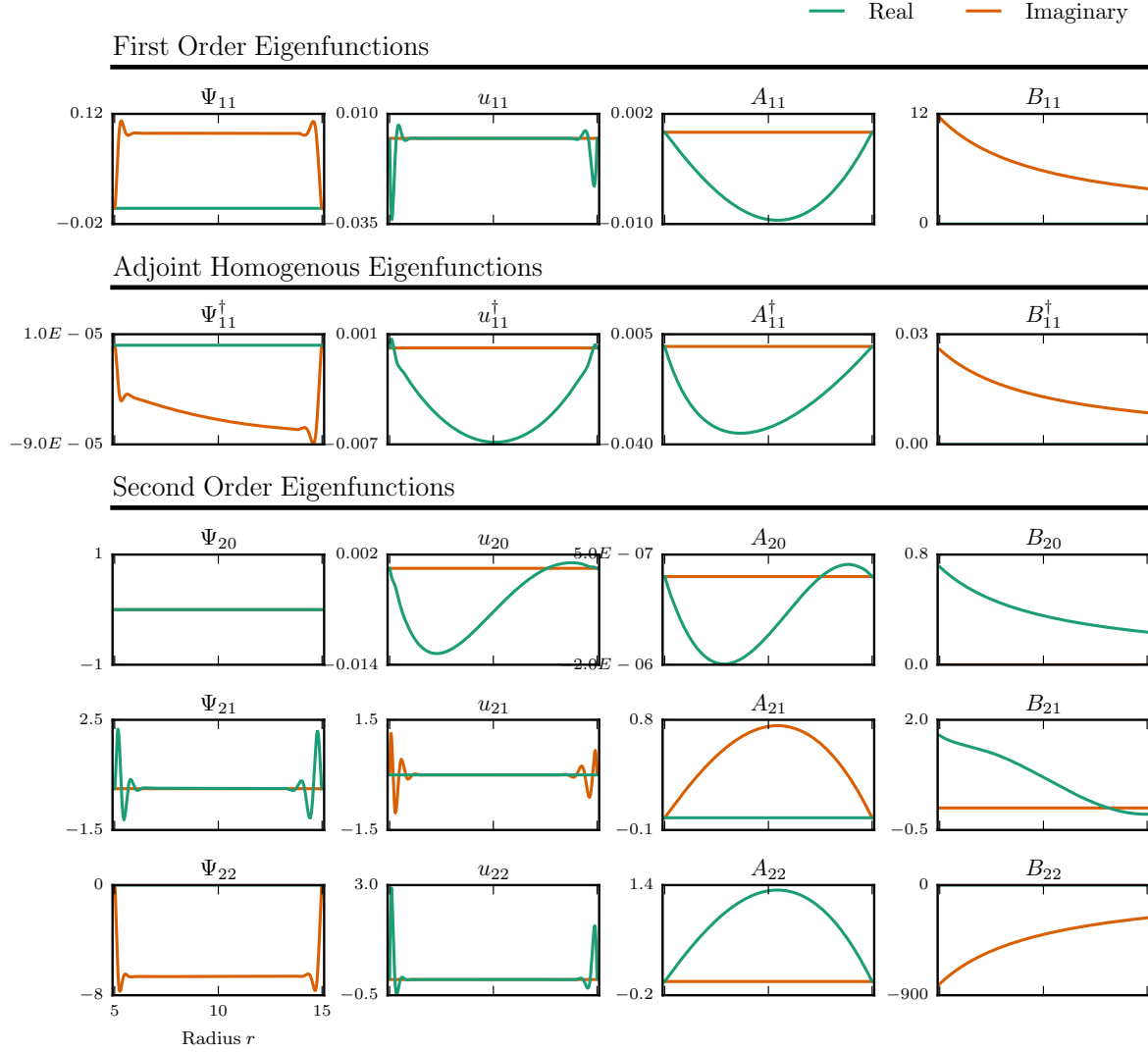


FIG. 2.— Eigenfunctions of the first order equations, first order adjoint homogenous equations, and second order equations. We use our fiducial parameters for the standard MRI ($\xi = 0$). First-order eigenfunctions are normalized such that they are either purely real or purely imaginary, and such that $\int \Psi_{11} dr = 1$. Adjoint homogenous eigenfunctions are normalized such that $\langle V_{11}^\dagger \cdot \mathcal{D}V_{11} \rangle = 1$.

equation. This amplitude equation decouples from the GLE because of the translational symmetry of the thin-gap geometry. Because that symmetry is not preserved in the wide-gap case, Umurhan et al. postulate that slow variation in the wide-gap geometry will be governed by two coupled amplitude equations. However, the purely geometric term in Equation 11 prevents the wide-gap geometry from sustaining a neutral mode. We note that a neutral mode of the form $B_\phi(r) \propto \frac{1}{r}$ would exist in a resistance-free approximation.

The preservation of symmetries in the thin-gap geometry is worth a closer look, as its absence in the wide gap case is the source of many differences in the systems. Latter et al. 2015 point out that in the ideal limit ($\nu, \eta \rightarrow 0$), the linearized system described by the lefthand side of Equations 8 - 11 can be expressed as a Shrödinger equation for the radial velocity. Similarly

combining equations to obtain a single expression for Ψ , we find that the thin-gap limit linear ideal MRI can be expressed as

$$\partial_x^2 \Psi + k_z^2 U(x) \Psi = 0 \quad (23)$$

where $U(x) = 3/v_A^2 k_z^2 + 1$ at marginality. When no-slip radial boundary conditions are applied, the thin-gap MRI system resembles a particle in a box with a radially constant potential well. Thus thin-gap linear MRI modes must be eigenstates of parity. These symmetries are preserved in the nonlinear MRI terms because they are nonlinear combinations of lower-order eigenfunctions. In the wide gap case, the “potential” $U(r)$ varies with r , so symmetric and antisymmetric modes are no longer required.

The nonlinear terms, detailed in Appendix B, represent an interesting departure from the thin-gap theory. The

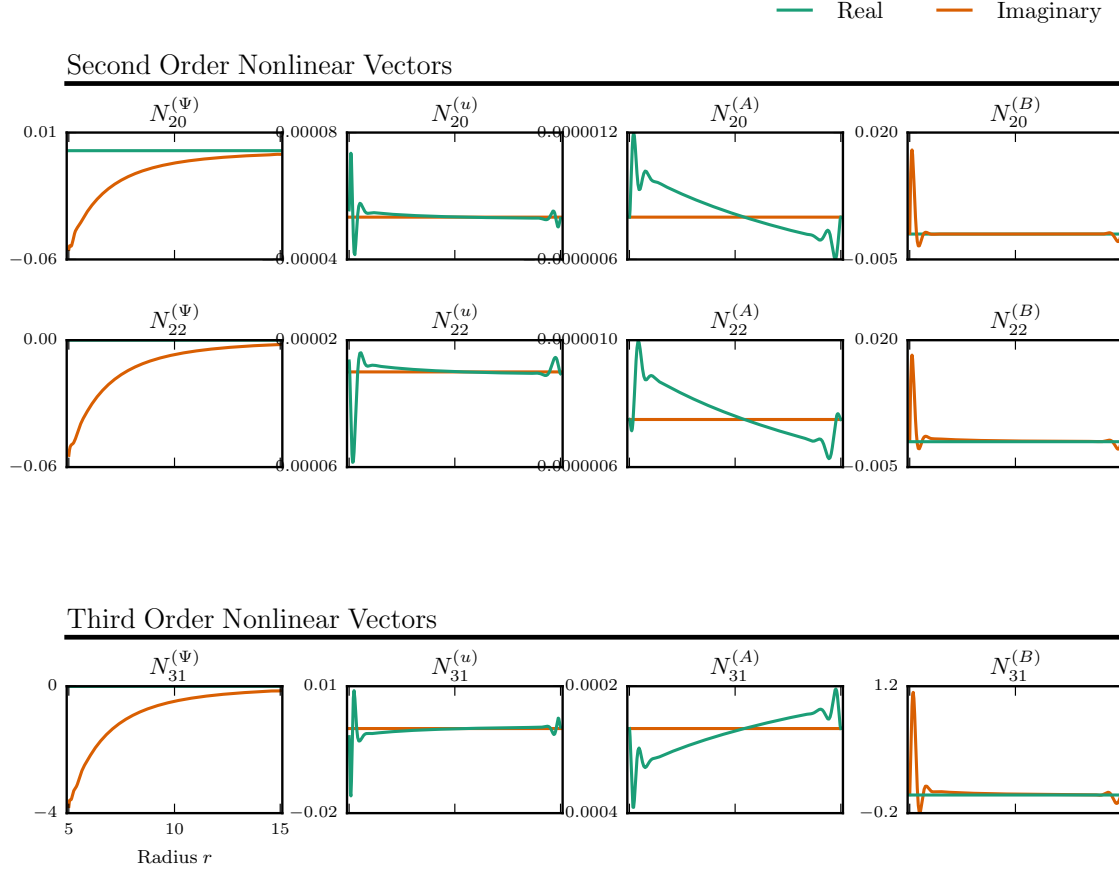


FIG. 3.— Nonlinear terms N_2 and N_3 for our fiducial standard MRI parameters.

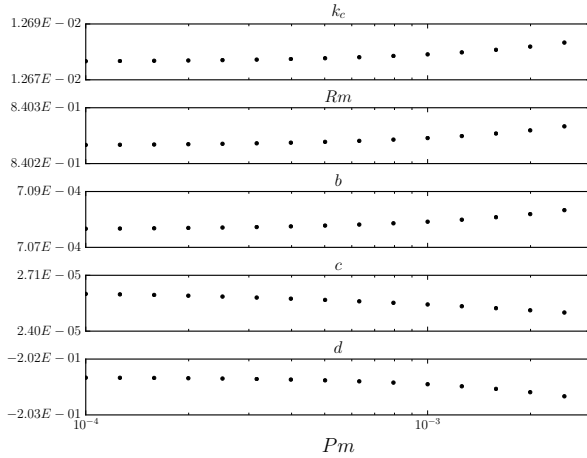


FIG. 4.— Critical parameters k_c and R_m , and coefficients of the Ginzburg-Landau equation (Equation 22) as a function of Pm . Note the very weak dependence of the coefficients on Pm . The saturation amplitude of the standard MRI system is very insensitive to Pm in the wide gap case.

thin-gap nonlinear terms at both second and third orders are linear combinations of Jacobians. The nonlinear terms in the wide-gap case differ from their thin-gap analogues with in the addition of vertical advective terms. These terms derive from the advective derivatives in the momentum and induction equations, but are filtered out in the thin-gap approximation. These advective terms allow the nonlinear contributions at both second and third order (i.e. N_2 and N_3) not to individually satisfy the boundary conditions on Ψ and u .

We examine the behavior of the wide gap MRI system as a function of Pm . Figure 4 shows the critical parameters k_c and R_m as a function of Pm , as well as the coefficients b , c , and d . The GLE coefficients are remarkably insensitive to Pm . From Equation 22 it is readily apparent that the asymptotic saturation amplitude is $\alpha_s = \pm\sqrt{b/c}$, so we conclude that the saturation amplitude of the MRI is only very weakly dependent on Pm . Note that because R_m is essentially constant as a function of Pm , the saturation amplitude is equivalently insensitive to Re^{-1} . This is in stark contrast to the narrow gap behavior of the system. For these same boundary conditions, Umurhan et al. (2007b) find that the narrow gap saturation amplitude scales as $Pm^{-4/3}$. They find that this amplitude dependence is driven by the $Pm^{1/3}$ dependence of the linear boundary layer. Boundary layer analysis similarly reveals a $\nu^{1/3}$ dependence for the radial extent of the boundary layer (Goodman & Ji 2002).

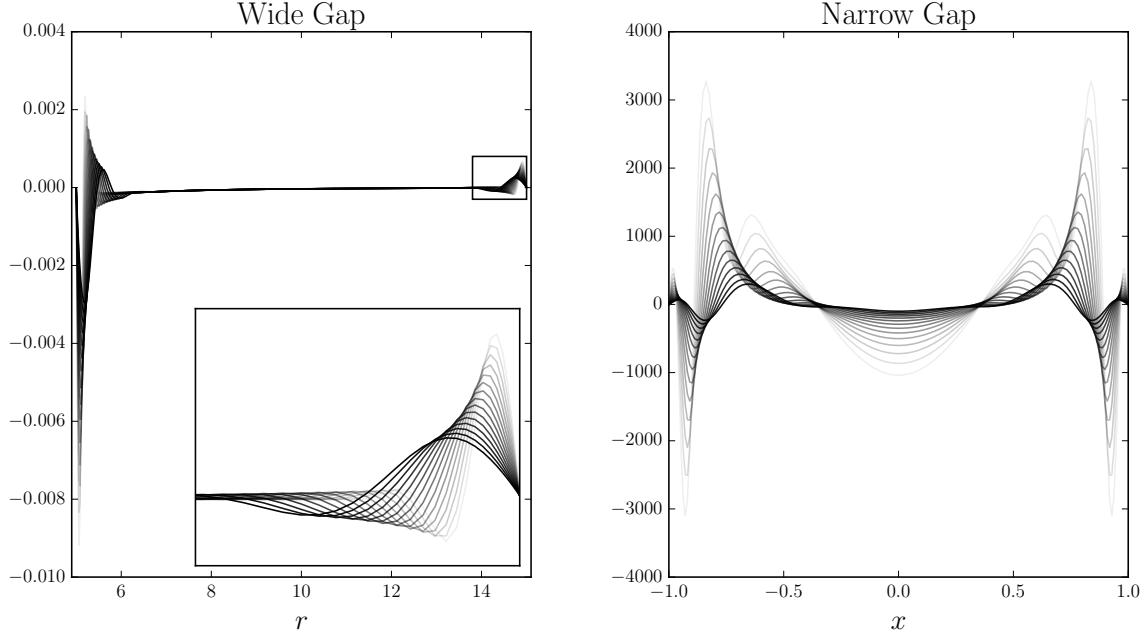


FIG. 5.— Nonlinear term $N_{31}^{(B)}$ for the wide gap (left) and narrow gap (right) standard MRI. Each line represents a run for a different Pm , from $Pm = 1E - 4$ (darkest) to $Pm \sim 1E - 3$ (lightest). Inlaid plot in wide gap case shows a zoomed-in view of the boundary layer at the outer boundary (r_2). In the narrow gap case the boundary layer strongly affects the bulk of the flow, while in the wide gap case the flow in the center of the channel is relatively unaffected by width of the boundary layers.

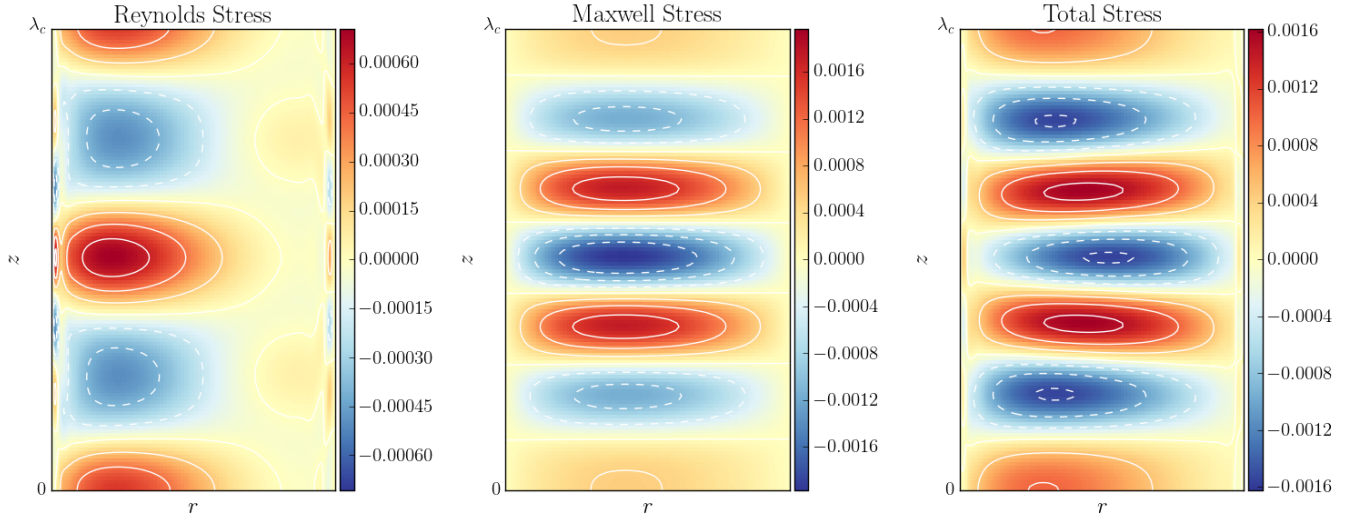


FIG. 6.— Reynolds ($\mathbb{T}_R = u_r u_\phi$), Maxwell ($\mathbb{T}_M = -\frac{2}{\beta} B_r B_\phi$), and total stress ($\mathbb{T} = \mathbb{T}_R + \mathbb{T}_M$) for the fiducial standard MRI case.

Why does the Pm scaling of the boundary layer width not translate to a stronger Pm scaling for the saturation amplitude in the wide gap case? The boundary layer in the wide gap case is strongly localized at the walls, i.e. r_1 and r_2 . Figure 5 shows the structure of the third-order nonlinear term $N_{31}^{(B)}$ as a function of Pm for both the narrow and wide gap standard MRI. N_{31} is the vector that determines the GLE coefficient c (see Appendix A for the wide gap case, and Umurhan et al. 2007b, Clark & Oishi 2016a for the narrow gap equations). Clearly, the boundary layers scale with Pm in both the wide and narrow gap MRI. However, in the narrow gap case this

scaling extends prominently into the center of the channel, whereas for the wide gap case the bulk of the flow is relatively unaffected by the boundary layer scaling.

4. CHANNEL MODES

Channel modes are radially independent linear MRI modes which are, under certain conditions, exact nonlinear solutions to the MRI equations.

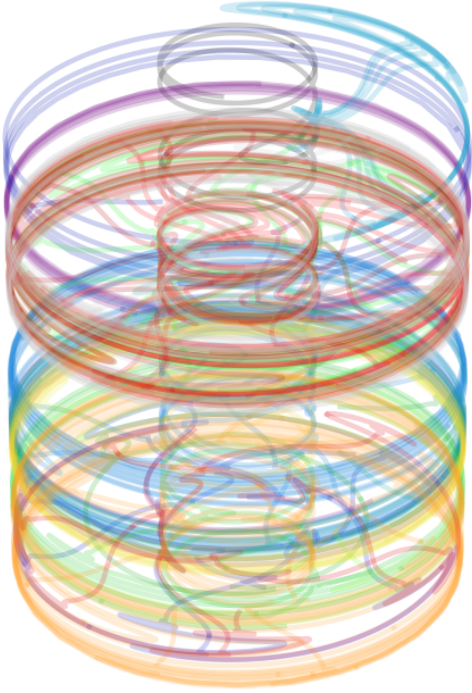


FIG. 7.— Visualization of the velocity perturbation field in the fiducial SMRI case. The three dimensional path of twenty randomly placed tracer particles is plotted, where the particle velocity is defined as the total (first + second order) velocity perturbation. This is meant to be a visualization only of the velocity field, so the particle motion feels no contribution from the magnetic field.

APPENDIX

A. DETAILED EQUATIONS

Here we detail the perturbation analysis described in Section 3. The linear system is described by Equation 17, where

$$\mathcal{L} = \mathcal{L}_0 + \mathcal{L}_1 \partial_z + \mathcal{L}_2 \partial_z^2 + \mathcal{L}_3 \partial_z^3 + \mathcal{L}_4 \partial_z^4, \quad (\text{A1})$$

$$\tilde{\mathcal{G}} = -\mathcal{G} \partial_z - \mathcal{L}_3 \partial_z^3, \quad (\text{A2})$$

$$\tilde{\mathcal{H}} = \mathcal{H} \partial_z, \quad (\text{A3})$$

and the constituent matrices are defined as

$$\mathcal{L}_0 = \begin{bmatrix} -\frac{1}{\text{Re}}(-\frac{3}{r^4} \partial_r + \frac{3}{r^3} \partial_r^2 - \frac{2}{r^2} \partial_r^3 + \frac{1}{r} \partial_r^4) & 0 & 0 & 0 \\ 0 & -\frac{1}{\text{Re}}(\partial_r^2 + \frac{1}{r} \partial_r - \frac{1}{r^2}) & 0 & 0 \\ 0 & 0 & -\frac{1}{\text{Rm}}(\partial_r^2 - \frac{1}{r} \partial_r) & 0 \\ 0 & 0 & 0 & -\frac{1}{\text{Rm}}(\partial_r^2 + \frac{1}{r} \partial_r - \frac{1}{r^2}) \end{bmatrix} \quad (\text{A4})$$

$$\mathcal{L}_1 = \begin{bmatrix} 0 & -\frac{2}{r} u_0 & \frac{2}{\beta}(\frac{1}{r^2} \partial_r - \frac{1}{r} \partial_r^2) & 0 \\ \frac{1}{r^2} u_0 + \frac{1}{r} \partial_r u_0 & 0 & 0 & -\frac{2}{\beta} \\ -1 & 0 & 0 & 0 \\ 0 & -1 & \frac{1}{r^2} u_0 - \frac{1}{r} \partial_r u_0 & 0 \end{bmatrix} \quad (\text{A5})$$

$$\mathcal{L}_2 = \begin{bmatrix} -\frac{1}{\text{Re}}(-\frac{2}{r^2} \partial_r + \frac{2}{r} \partial_r^2) & 0 & 0 & 0 \\ 0 & -\frac{1}{\text{Re}} & 0 & 0 \\ 0 & 0 & -\frac{1}{\text{Rm}} & 0 \\ 0 & 0 & 0 & -\frac{1}{\text{Rm}} \end{bmatrix} \quad (\text{A6})$$

$$\mathcal{L}_3 = \begin{bmatrix} 0 & 0 & -\frac{2}{\beta} \frac{1}{r} & 0 \\ 0 & 0 & 0 & 0 \\ 0 & 0 & 0 & 0 \\ 0 & 0 & 0 & 0 \end{bmatrix} \quad (\text{A7})$$

$$\mathcal{L}_4 = \begin{bmatrix} -\frac{1}{\text{Re}} \frac{1}{r} & 0 & 0 & 0 \\ 0 & 0 & 0 & 0 \\ 0 & 0 & 0 & 0 \\ 0 & 0 & 0 & 0 \end{bmatrix} \quad (\text{A8})$$

$$\mathcal{G} = \begin{bmatrix} 0 & 0 & \frac{2}{\beta}(\frac{1}{r^2} \partial_r - \frac{1}{r} \partial_r^2) & 0 \\ 0 & 0 & 0 & -\frac{2}{\beta} \\ -1 & 0 & 0 & 0 \\ 0 & -1 & 0 & 0 \end{bmatrix} \quad (\text{A9})$$

$$\mathcal{H} = \begin{bmatrix} 0 & 0 & 0 & \frac{2}{\beta} \frac{2}{r^2} \\ 0 & 0 & 0 & 0 \\ 0 & 0 & 0 & 0 \\ -\frac{2}{r^3} & 0 & 0 & 0 \end{bmatrix} \quad (\text{A10})$$

$$\mathcal{D} = \begin{bmatrix} \frac{1}{r} \partial_r^2 + \frac{1}{r} \partial_z^2 - \frac{1}{r^2} \partial_r & 0 & 0 & 0 \\ 0 & 1 & 0 & 0 \\ 0 & 0 & 1 & 0 \\ 0 & 0 & 0 & 1 \end{bmatrix} \quad (\text{A11})$$

B. NONLINEAR TERMS

Here we detail the perturbative expansion of the nonlinear vector \mathbf{N} in Equation 17.

$$\mathbf{N} = \epsilon^2 \mathbf{N}_2 + \epsilon^3 \mathbf{N}_3 \quad (\text{B1})$$

$$N_2^\Psi = J(\Psi_1, \frac{1}{r^2} \nabla^2 \Psi_1) + J(\Psi_1, -\frac{2}{r^3} \partial_r \Psi_1) - \frac{2}{\beta} J(A_1, \frac{1}{r^2} \nabla^2 A_1) - \frac{2}{\beta} J(A_1, -\frac{2}{r^3} \partial_r A_1) - \frac{2}{r} u_1 \partial_z u_1 + \frac{2}{\beta} \frac{2}{r} B_1 \partial_z B_1 \quad (\text{B2})$$

$$N_2^u = \frac{1}{r} J(\Psi_1, u_1) - \frac{1}{r} \frac{2}{\beta} J(A_1, B_1) + \frac{1}{r^2} u_1 \partial_z \Psi_1 - \frac{2}{\beta} \frac{1}{r^2} B_1 \partial_z A_1 \quad (\text{B3})$$

$$N_2^A = -\frac{1}{r} J(A_1, \Psi_1) \quad (\text{B4})$$

$$N_2^B = -\frac{1}{r} J(A_1, u_1) - \frac{1}{r} J(B_1, \Psi_1) - \frac{1}{r^2} B_1 \partial_z \Psi_1 + \frac{1}{r^2} u_1 \partial_z A_1 \quad (\text{B5})$$

$$\begin{aligned} N_3^\Psi = & J(\Psi_1, \frac{1}{r^2} \nabla^2 \Psi_2) + J(\Psi_2, \frac{1}{r^2} \nabla^2 \Psi_1) + 2J(\Psi_1, \frac{1}{r^2} \partial_Z \partial_z \Psi_1) + J(\Psi_1, -\frac{2}{r^3} \partial_r \Psi_2) + J(\Psi_2, -\frac{2}{r^3} \partial_r \Psi_1) \\ & + \tilde{J}(\Psi_1, \frac{1}{r^2} \nabla^2 \Psi_1) + \tilde{J}(\Psi_1, -\frac{2}{r^3} \partial_r \Psi_1) - \frac{2}{\beta} J(A_1, \frac{1}{r^2} \nabla^2 A_2) - \frac{2}{\beta} J(A_2, \frac{1}{r^2} \nabla^2 A_1) - \frac{4}{\beta} J(A_1, \frac{1}{r^2} \partial_Z \partial_z A_1) \\ & - \frac{2}{\beta} J(A_1, -\frac{2}{r^3} \partial_r A_2) - \frac{2}{\beta} J(A_2, -\frac{2}{r^3} \partial_r A_1) - \frac{2}{\beta} \tilde{J}(A_1, \frac{1}{r^2} \nabla^2 A_1) - \frac{2}{\beta} \tilde{J}(A_1, -\frac{2}{r^3} \partial_r A_1) \\ & - \frac{2}{r} u_1 \partial_z u_2 - \frac{2}{r} u_2 \partial_z u_1 - \frac{2}{r} u_1 \partial_z u_1 + \frac{2}{\beta} \frac{2}{r} B_1 \partial_z B_2 + \frac{2}{\beta} \frac{2}{r} B_2 \partial_z B_1 + \frac{2}{\beta} \frac{2}{r} B_1 \partial_z B_1 \end{aligned} \quad (\text{B6})$$

$$\begin{aligned} N_3^u = & \frac{1}{r} J(\Psi_1, u_2) + \frac{1}{r} J(\Psi_2, u_1) + \frac{1}{r} \tilde{J}(\Psi_1, u_1) - \frac{1}{r} \frac{2}{\beta} J(A_1, B_2) - \frac{1}{r} \frac{2}{\beta} J(A_2, B_1) - \frac{1}{r} \frac{2}{\beta} \tilde{J}(A_1, B_1) \\ & + \frac{1}{r^2} u_1 \partial_z \Psi_2 + \frac{1}{r^2} u_2 \partial_z \Psi_1 + \frac{1}{r^2} u_1 \partial_z \Psi_1 - \frac{2}{\beta} \frac{1}{r^2} B_1 \partial_z A_2 - \frac{2}{\beta} \frac{1}{r^2} B_2 \partial_z A_1 - \frac{2}{\beta} \frac{1}{r^2} B_1 \partial_z A_1 \end{aligned} \quad (\text{B7})$$

$$N_3^A = -\frac{1}{r} J(A_1, \Psi_2) - \frac{1}{r} J(A_2, \Psi_1) - \frac{1}{r} \tilde{J}(A_1, \Psi_1) \quad (\text{B8})$$

$$\begin{aligned} N_3^B = & -\frac{1}{r} J(A_1, u_2) - \frac{1}{r} J(A_2, u_1) - \frac{1}{r} \tilde{J}(A_1, u_1) - \frac{1}{r} J(B_1, \Psi_2) - \frac{1}{r} J(B_2, \Psi_1) - \frac{1}{r} \tilde{J}(B_1, u_1) \\ & - \frac{1}{r^2} B_1 \partial_z \Psi_2 - \frac{1}{r^2} B_2 \partial_z \Psi_1 - \frac{1}{r^2} B_1 \partial_z \Psi_1 + \frac{1}{r^2} u_1 \partial_z A_2 + \frac{1}{r^2} u_2 \partial_z A_1 + \frac{1}{r^2} u_1 \partial_z A_1 \end{aligned} \quad (\text{B9})$$

REFERENCES

- Aranson, I.S. & Kramer, L., 2002, Rev. Mod. Phys. 74, 99
 Armitage, P. 2010, ARA&A, 49, 195
 Balbus, S A and Hawley, J F, 1991, The Astrophysical Journal, 376, 214
 Chandrasekhar, S. 1960, Proceedings of the National Academy of Sciences of the United States of America, 46, 253
 Clark, S.E. and Oishi, J.S., 2016, in prep
 Cross, M. C., & Hohenberg, P. C., 1993, Rev. Mod. Phys. 65, 851
 Ebrahimi, F., Prager, S.C., Schnack, D.D
 Gissinger, C, Ji, H, Goodman, J, 2011, Phys. Rev. E 84, 026308
 Gissinger, C, Goodman, J, & Ji, H, 2012, Physics of Fluids 24, 074109
 Goodman, J. & Ji, H., 2002, JFM, 462, 365
 Goodman, J, Xu, G, 1994, ApJ, 432, 213
 Hollerbach, R, Proc. R. Soc. A, 2009, 465, 2107
 Hollerbach, R. & Rüdiger, G., 2005, Phys. Rev. Lett. 95, 124501
 Ji, H, Goodman, J, Kageyama, A, Mon. Not. R. Astron. Soc., 2001, 325, 1
 Kirillov, O, & Stefani, F, 2013, Phys. Rev. Lett. 111, 061103
 Knobloch, E, Julien K, 2005, Physics of Fluids, 17, 094106
 Latter, H.N., Fromang, S., & Faure, J., 2015, MNRAS 453, 3257
 Lesur, G., Ferreira, J., & Ogilvie, G. I. 2013, A&A 550, A61
 Liu, W, Goodman, J, Herron, I, and Ji, H, 2006, Phys. Rev. E 74, 056302
 Pessah, M, 2010, ApJ, 716, 1012
 Rüdiger, G, & Hollerbach, R, Phys. Rev. E 76, 068301
 Schartman, E, Ji, H, Burin, M J, Rev Sci Instrum, 2009, 80, 024501
 Sisan, D R, Mujica, N, Tillotson, W A, Huang Y-M, Dorland, W, Hassam, A B, Antonsen, T M, Lathrop, D P, Phys Rev Lett, 2004, 93, 11
 Stefani, F, Gundrum, T, Gerbeth, G, Rüdiger, G, Schultz, M, Szklarski, J, Hollerbach, R, Phys Rev Lett, 2006, 97, 184502
 Stefani, F, Gerbeth, G, Gundrum, T, Hollerbach, R, Priede, J, Rüdiger, G, and Szklarski, J, Phys Rev E, 80, 066303
 Umurhan, O.M., Regev, O., Menou, K., 2007, Phys. Rev. Letters, 98, 034501
 Umurhan, O.M., Regev, O., Menou, K., 2007, Phys. Rev. E, 76, 036310